Efficient Monte Carlo simulation of spatio-temporal speckles and their correlations

Chen Bar[1,*], **Ioannis Gkioulekas**[2], **and Anat Levin**[1]

[1] *Department of Electrical and Computer Engineering, Technion, Haifa, Israel*
[2] *Robotics Institute, Carnegie Mellon University, PA, USA*
[*] *Corresponding author: chen.bar@campus.technion.ac.il*

Compiled July 30, 2023

When viewed under coherent illumination, scattering materials such as tissue exhibit highly varying speckle patterns. Despite their noise-like appearance, the temporal and spatial variations of these speckles, resulting from internal tissue dynamics and/or external perturbation of the illumination, carry strong statistical information that is highly valuable for tissue analysis. The full practical applicability of these statistics is still hindered by the difficulty of simulating these speckles and their statistics. This paper proposes an efficient Monte Carlo framework that can efficiently sample physically-correct speckles and estimate their covariances. While Monte Carlo algorithms were originally derived for incoherent illumination, our approach simulates complex-valued speckle fields. We compare the statistics of our speckle fields against those produced by an exact numerical wave solver and show a precise agreement, while our simulator is a few orders of magnitude faster and scales to much larger scenes. We also show that the simulator predictions accurately align with existing analytical models and simulation strategies, which currently address various partial settings of the general problem.

http://dx.doi.org/10.1364/optica.XX.XXXXXX

1. INTRODUCTION

When a camera images a scattering volume illuminated by coherent light, captured images are characterized by pseudo-random patterns called speckle. Despite their noise- like appearance, speckle patterns have strong statistical properties that provide rich information about the scattering material that is being imaged. These statistical properties have been studied extensively in optics [1–11], and form the basis for many imaging techniques in application areas where scattering is important, such as medical imaging and remote sensing.

In the past, speckle statistics has been studied in two disjointed contexts: spatial and temporal. Temporal speckle statistics [12, 13] are mostly used for imaging liquid dispersions [14, 15] or temporally varying blood vessels [16] deep inside tissue, in techniques like diffuse correlation spectroscopy [17–22], laser speckle contrast imaging [12, 23, 24], and dynamic light scattering [25, 26]. The study of these statistics attempts to analyze *motion* in the volume. The idea is based on a set of theoretical results relating the temporal variation of speckle intensity to the particle (blood-cell) motion speed inside the tissue, and on a diffusion relation connecting the speed of Brownian motion to particle properties. At the same time, speckles exhibit important spatial correlations. For example, speckle images are approximately shift-invariant with respect to small perturbations of illumination, a property known as the *memory effect* (ME). This property has been exploited in a variety of applications, including seeing through a scattering layer and behind corners [27–36], measuring intrinsic material parameters [37], as well as adaptive-optics focusing of light through highly-aberrated materials [10, 11, 38].

Despite much research on temporal *or* spatial statistics, there is little usage of joint spatio-temporal statistics, in part due to limited understanding of such statistics, and due to the lack of good simulation tools. While the most accurate way to compute such statistics would involve exact solutions to the wave equations [39–41], such solvers are computationally prohibitive and can only handle toy scenes. One popular large-scale approach [42] exploits Monte Carlo (MC) algorithms for the simulation of *positive* temporal-only correlations, at a fixed sensor location and under fixed illumination conditions. However, the simulation of spatio-temporal correlations between measurements at different positions was not addressed.

This paper offers two main contributions. First, we develop MC algorithms for the evaluation of *complex spatio-temporal* correlations. Second, beyond computing statistics, we can *sample complex-valued speckle fields* with physically-correct statistics. These fields can be thought of as realizations of spatio-temporal transmission matrices whose second order statistics are indistinguishable from those produced by an exact solution to the wave equation. As we show below, this new ability is highly valuable in the design of tissue imaging algorithms, and in particular in the training of machine-learning systems [43, 44].

To this end we build on our recent MC rendering framework [45, 46], computing the *spatial* correlations between speckle fields measured at different sensor positions and under varying illumination conditions. We extend this for the evaluation of *spatio-temporal* correlations. Beyond computing pairwise correlations, the approach can realize complex speckle fields with accurate covariance statistics.

We compare our approach against a previous MC toolbox [42] for computing temporal-only speckle correlations, and we also validate the spatio-temporal correlations against an exact wave solver in flatland.

We demonstrate two possible applications of such spatio-temporal correlations. The first application scenario has to do with motion tracking. It is usually believed that blood motion is a combination of Brownian motion in a random direction and a directional flow along the vessel direction. However, the temporal speckle literature evaluates mostly the Brownian component. While there is evidence that in certain applications the Brownian component is indeed dominant, there are fewer attempts to study application scenarios with dominant directional motion, in part due to the difficulty in simulating such correlations. This is due to the fact that the directional motion is manifested as a spatio-temporal correlation rather than a temporal-only effect, since a cell that is imaged at pixel x and time t would be imaged at a neighboring spatial pixel $x + \Delta_x$ at a successive time frame. With our approach, we show for the first time how to simulate this effect and how to disentangle the directional and Brownian motion components.

In a second application, we revisit a recent empirical study on dynamic wavefront shaping [47], where different approaches for computing a wavefront correction are compared in a medium consisting of a combination of static and dynamic scattering layers. It has been suggested that iterative wavefront shaping algorithms effectively correct mostly the static aberrations and thus they are more stable over time. While the results in [47] are based on an experimental setup, our approach can synthesize spatio-temporal transmission matrices with the correct statistics. With such transmission matrices, we can simulate the setup of [47] and re-validate their observation in a simple numerical simulation, which can be more easily generalized to a large class of scenes and materials.

Our simulator will be made publicly available on Github.

2. MODELING SPECKLE STATISTICS

Setting and notation. We denote three-dimensional vectors (e.g., points $\mathbf{o}, \mathbf{i}, \mathbf{v}$) with bold letters, and denote unit vectors with a circumflex (e.g., directions $\hat{\omega}, \hat{\mathbf{i}}, \hat{\mathbf{v}}$). We denote the unit vector from $\mathbf{y}$ to $\mathbf{o}$ as $\widehat{\mathbf{yo}}$. We assume the illumination is *fully-coherent* and *unpolarized*. Our sources and sensors can be either points $\mathbf{i}, \mathbf{v}$ or directions $\hat{\mathbf{i}}, \hat{\mathbf{v}}$. We often use point notation $\mathbf{i}, \mathbf{v}$ for both cases, except where context requires otherwise.

We consider scattering volumes $\mathcal{V} \in \mathbb{R}^3$ satisfying a few common assumptions [48]: First, the average distance between scatterers is an order of magnitude larger than the wavelength. Second, the locations of scatterers are statistically independent. Third, the motions of different scatterers are statistically independent, and their average displacement is an order of magnitude smaller than the distance between scatterers. Finally, we ignore refraction and reflection events at the interface of volume $\mathcal{V}$.

Bulk material properties. The optical properties of scattering materials can be summarized by a few statistical parameters. The extinction coefficient σ_t of the material governs the density of scatterers in the volume. It can be decomposed as $\sigma_t = \sigma_s + \sigma_a$, where the scattering and absorption coefficients σ_s and σ_a model the portion of energy that is scattered and absorbed upon interaction with a scatterer. The mean free path is the average distance in the volume that light travels between two scattering events, and it can be shown to be inversely proportional to the extinction coefficient $MFP = 1/\sigma_t$. The complex scattering amplitude function $s(\cos\theta)$ describes how a field interacts with a scatterer: if a scatterer is illuminated from direction $\hat{\mathbf{i}}$, the scattered field u at direction $\hat{\mathbf{v}}$ is proportional to $s(\hat{\mathbf{i}} \cdot \hat{\mathbf{v}})$. The phase function is defined as $\rho(\cos\theta) \equiv |s(\cos\theta)|^2$.

Motion parameterization. Scatterers are moving independently with displacements following a distribution $\mathcal{T}(\mathbf{\Delta_t})$. We model it as a Brownian motion with a drift, so that

$$\mathbf{\Delta_t} = t \cdot \mathbf{U} + \mathbf{w}\sqrt{2D|t|}, \tag{1}$$

where $\mathbf{w}$ is sampled from a 3-dimensional unit normal distribution, and the scalar t is the time interval of the displacement. The above motion has two components: an isotropic Brownian motion with a diffusion coefficient D with the dimensions cm^2/s, corresponding to fluctuations of the particles in all directions, and a mean direction $\mathbf{U}$ which encodes the constant velocity flow along the vessel direction. The corresponding mean and variance of the 3D temporal displacement are

$$\mathrm{E}\left[\mathbf{\Delta_t}\right] = t \cdot \mathbf{U}, \quad \mathrm{E}\left[\left\|\mathbf{\Delta_t} - \mathrm{E}\left[\mathbf{\Delta_t}\right]\right\|^2\right] = 6D|t|. \tag{2}$$

In thick tissue where the light crosses multiple vessels with varying orientations, the flow direction often reduces into an isotropic perturbation known as “random motion” [16, 49], whose variance scales as a function of t^2 rather than as a function of t as the Brownian component. For accuracy we chose to model this random motion with a mean displacement $\mathbf{U}$, where the direction of $\mathbf{U}$ is spatially varying (different $\mathbf{U}$ vectors in different volumetric positions).

For ease of notation, the derivation below assumes that scattering volumes are spatially homogeneous, meaning that scatterers are uniformly distributed, or equivalently, that the bulk parameters as well as the motion parameters are the same everywhere inside a volume. In practice this assumption can be easily removed and our implementation does take into account heterogeneous spatial variation (and in particular, varying $\mathbf{U}$ vectors).

Speckle statistics. We now consider a volume with multiple scatterers as in Fig. 1(a): We denote the time-dependent position of scatterers in the volume as $O(t) = \{\mathbf{o}_1(t), \mathbf{o}_2(t), \ldots\}$. The position $\mathbf{o}_b(0)$ of each scatterer at time 0 is sampled *independently* from other scatterers, from the bulk material density. Then, scatterer displacements are sampled independently from $\mathcal{T}(\mathbf{\Delta_t})$. Scatterer position at time t is:

$$\mathbf{o}_b(t) = \mathbf{o}_b\,(0) + \mathbf{\Delta}_{\mathbf{t}b}. \tag{3}$$

Scatterers are illuminated from a source $\mathbf{i}$, and imaged with a sensor $\mathbf{v}$. Knowing the exact scatterer locations at every time step, we can solve the wave equation to obtain the complex-valued scattered field $u_{\mathbf{v}}^{\mathbf{i},O}(t)$, which typically contains large fluctuations with a semi-random noise structure known as speckles (see flatland speckles in Fig. 1(b,c)). A camera usually only measures the intensity of these fields $I_{\mathbf{v}}^{\mathbf{i},O}(t) = |u_{\mathbf{v}}^{\mathbf{i},O}(t)|^2$.

To capture speckle statistics, we can begin with the *speckle mean*,

$$m_{\mathbf{v}}^{\mathbf{i}}(t) = \mathrm{E}_{O(t)}\left[u_{\mathbf{v}}^{\mathbf{i},O}(t)\right]. \tag{4}$$

Assuming scatterer density is stationary, the speckle mean is time-invariant and we shorten notation and denote it as $m_{\mathbf{v}}^{\mathbf{i}}$.

We can similarly define higher-order statistics of speckles. Of particular importance will be the *speckle covariance*,

$$C_{\mathbf{v}_1,\mathbf{v}_2}^{\mathbf{i}_1,\mathbf{i}_2}(t_1,t_2) = \mathrm{E}_{O(t_1,t_2)}\left[u_{\mathbf{v}_1}^{\mathbf{i}_1,O}(t_1)\cdot u_{\mathbf{v}_2}^{\mathbf{i}_2,O}(t_2)^*\right] - m_{\mathbf{v}_1}^{\mathbf{i}_1}\cdot {m_{\mathbf{v}_2}^{\mathbf{i}_2}}^*, \tag{5}$$

where $(\cdot)^*$ denotes complex conjugation. In this case, $u_{\mathbf{v}_1}^{\mathbf{i}_1,O}(t_1), u_{\mathbf{v}_2}^{\mathbf{i}_2,O}(t_2)$ are two speckle fields generated by the *same* scatterer configuration at two time instances. The scatterer instantiations are illuminated by two incident waves from $\mathbf{i}_1, \mathbf{i}_2$, and measured at two sensors $\mathbf{v}_1, \mathbf{v}_2$.

As we discuss in supplement, the speckle mean can be computed using a closed-form expression; in fact, because the speckle mean is the aggregate of complex numbers of essentially randomly-varying phase, it is typically zero (unless ballistic light is present). Therefore, when characterizing speckle statistics, the most challenging part is computing the covariance.

Note that our goal in this paper is to compute covariances between *complex* speckle fields. Such covariances can be easily translated to covariances of positive intensity images. Assuming the speckles follow a zero-mean multi-variate Gaussian distribution, the Siegert relation can be used:

$$\mathrm{E}_{O(t_1,t_2)}\left[I_{\mathbf{v}^1}^{\mathbf{i}_1,O}(t_1)\cdot I_{\mathbf{v}^2}^{\mathbf{i}_2,O}(t_2)\right] - \mathrm{E}_{O(t_1)}\left[I_{\mathbf{v}^1}^{\mathbf{i}_1,O}(t_1)\right]\cdot \mathrm{E}_{O(t_2)}\left[I_{\mathbf{v}^2}^{\mathbf{i}_2,O}(t_2)\right] = |C_{\mathbf{v}_1,\mathbf{v}_2}^{\mathbf{i}_1,\mathbf{i}_2}(t_1,t_2)|^2. \tag{6}$$

Computing speckle statistics. A straightforward approach for computing the speckle covariance is to sample N different scatterer configurations $O^1(t), \dots O^N(t)$, solve the wave equation for each configuration at each time instance , and then compute the empirical covariance:

$$C_{\mathbf{v}_1,\mathbf{v}_2}^{\mathbf{i}_1,\mathbf{i}_2}(t_1,t_2) \approx \frac{1}{N}\sum_{n=1}^{N} u_{\mathbf{v}_1}^{\mathbf{i}_1,O^n}(t_1)\cdot u_{\mathbf{v}_2}^{\mathbf{i}_2,O^n}(t_2)^* - m_{\mathbf{v}_1}^{\mathbf{i}_1}\cdot {m_{\mathbf{v}_2}^{\mathbf{i}_2}}^*. \tag{7}$$

Fig. 1(d-f) shows speckle covariances evaluated with this procedure. However, solving the wave equation is only tractable for a very small number of particles (a few thousands), and this computational cost is further exacerbated by the need to repeat this process multiple times. Our goal is to devise Monte Carlo algorithms that can compute *the same* speckle covariance much more efficiently.

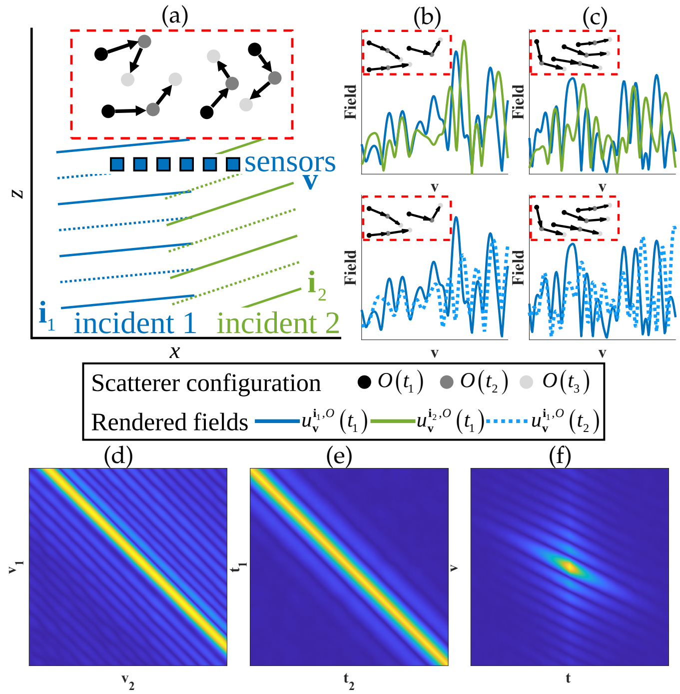

Fig. 1. Speckle correlations: (a)Flatland geometry illustration: we consider a volume with moving scatterers, under two illumination directions, and measure the resulting field on a planar sensor. (b-c) Given a statistical description of bulk material parameters, we can sample multiple scatterer instantiations, and (b,c) illustrate two such instantiations. Below each scatterer instantiation we plot the speckle field obtained by solving the wave equation under two incident illuminations and at two time instances. (d-f) illustrate some correlations in the data. (d) Spatial covariance $c(\mathbf{v}_1,\mathbf{v}_2) = \mathrm{E}\left[u_{\mathbf{v}_1}^{\mathbf{i}_1}(t_o)\cdot u_{\mathbf{v}_2}^{\mathbf{i}_2}(t_o)^*\right]$, note the strong correlation along a diagonal shifted from the center. This is the memory effect correlation, as speckles generated under nearby illuminations are correlated but *shifted*. (e) Temporal-only covariance for a fixed illumination $\mathbf{i}_o$ and a fixed sensor point $\mathbf{v}_o$: $c(t_1,t_2) = \mathrm{E}\left[u_{\mathbf{v}_o}^{\mathbf{i}_o}(t_1)\cdot u_{\mathbf{v}_o}^{\mathbf{i}_o}(t_2)^*\right]$. At the same time instance the speckle fields are most similar, which is manifested by a strong diagonal in the correlation matrix. As the time difference increases, the speckles start to change. (f) Spatio- temporal covariance, where one wave is fixed and the other varies at both space and time: $c(\mathbf{v},t) = \mathrm{E}\left[u_{\mathbf{v}_o}^{\mathbf{i}_o}(t_o)\cdot u_{\mathbf{v}}^{\mathbf{i}_o}(t)^*\right]$. The correlation is strongest at the central spot $t = t_o, \mathbf{v} = \mathbf{v}_o$ where the two waves are identical, but it has a strong elongated diagonal corresponding to a non-zero constant velocity component $\mathbf{U}$ in the scatterer motion.

3. PATH-INTEGRAL FORMULATION

The basis for a Monte Carlo evaluation of speckle covariance is expressing it as an integral of paths through the scattering volume, and then approximating this integral by importance-sampling many such paths, summing their contributions. These path integrals can be justified by the Twersky approximation [50, 51] and the correlation-transfer equation (CTE) [52], which extends the well known radiative-transfer equation (RTE) describing intensity propagation in a scattering media, to describe the covariance of complex fields. To simplify the flow of

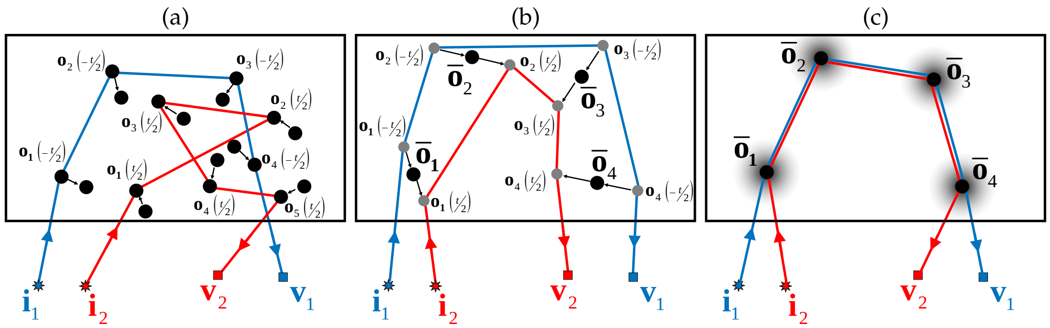

Fig. 2. Path pairs for speckle covariance: (a) A naive approach for computing speckle covariance should integrate path contributions over all pairs of paths from $\mathbf{i}_1$ to $\mathbf{v}_1$ and from $\mathbf{i}_2$ to $\mathbf{v}_2$. However most such paths have random phases and do not contribute to the correlation. (b) Covariance estimate can be reduced by considering only path pairs sharing all their nodes. Note that if we are computing correlations at two different time instances t_1, t_2, the path $\vec{\mathbf{x}}^1$ traces the position of the scatterer at time instance t_1 and the path $\vec{\mathbf{x}}^2$ traces its position at time t_2. (c) We can further simplify the covariance estimate and consider only the mean paths. Around each node in the path we analytically integrate the contribution of all possible motions.

the main text we provide the full derivation in supplement and only summarize here the main results.

For ease of notation, w.l.o.g we consider covariances between two time instances of the form $t_1 = -t/2, t_2 = t/2$. We denote the mean particle position by

$$\bar{\mathbf{o}} = \frac{1}{2}\left(\mathbf{o}\left(t_1\right) + \mathbf{o}\left(t_2\right)\right), \tag{8}$$

so that $\mathbf{o}\left(t_1\right) = \bar{\mathbf{o}} - 1/2\boldsymbol{\Delta}_\mathbf{t}$, $\mathbf{o}\left(t_2\right) = \bar{\mathbf{o}} + 1/2\boldsymbol{\Delta}_\mathbf{t}$.

We start by defining a mean path through the volume as an ordered sequence

$$\vec{\mathbf{x}}^s = \bar{\mathbf{o}}_1 \to \ldots \to \bar{\mathbf{o}}_B, \quad \bar{\mathbf{o}}_1, \ldots, \bar{\mathbf{o}}_B \in \mathcal{V}, \tag{9}$$

where $B \in \{1, \ldots, \infty\}$ and we consider a pair of paths from $\hat{\mathbf{i}}_1$ to $\mathbf{v}^1$ and from $\hat{\mathbf{i}}_2$ to $\mathbf{v}^2$ that share all their intermediate nodes, and differ only in the start/end segments connecting them to the source/sensor, see Fig. 2(c):

$$\vec{\mathbf{x}}^1 = \mathbf{i}_1 \to \vec{\mathbf{x}}^s \to \mathbf{v}_1, \quad \vec{\mathbf{x}}^2 = \mathbf{i}_2 \to \vec{\mathbf{x}}^s \to \mathbf{v}_2, \tag{10}$$

Our main result, proven in supplementary, is in showing that the covariance can be expressed as the integral over the space of such joint path pairs

$$C^{\mathbf{i}_1,\mathbf{i}_2}_{\mathbf{v}_1,\mathbf{v}_2}\left(\text{-}\tfrac{t}{2}, \tfrac{t}{2}\right) = \int_{\mathbb{P}} c_{\vec{\mathbf{x}}^s}\left(\text{-}\tfrac{t}{2}, \tfrac{t}{2}\right)\, \mathrm{d}\vec{\mathbf{x}}^s, \tag{11}$$

where each path has a contribution that can be expressed as a Markovian product of its segments

$$c_{\vec{\mathbf{x}}^s}\left(\text{-}\tfrac{t}{2}, \tfrac{t}{2}\right) = \prod_{b=0}^{B} f_b^I. \tag{12}$$

The contribution of central segments is identical to the contribution considered by classical Monte Carlo algorithms for evaluating temporal-only correlations [42]:

$$\begin{aligned} f_b^I =& \gamma(\widehat{\bar{\mathbf{o}}_b, \bar{\mathbf{o}}_{b+1}} - \widehat{\bar{\mathbf{o}}_{b-1}, \bar{\mathbf{o}}_b}) \cdot \rho(\widehat{\bar{\mathbf{o}}_{b-1}\bar{\mathbf{o}}_b} \cdot \widehat{\bar{\mathbf{o}}_b\bar{\mathbf{o}}_{b+1}}) \\ &\cdot \tilde{\alpha}(\bar{\mathbf{o}}_b, \bar{\mathbf{o}}_{b+1})^2 \cdot \sigma_s(\bar{\mathbf{o}}_{b+1}) \qquad \text{for } 2 \le b \le B-1, \end{aligned} \tag{13}$$

and the formula for the start end/segments (the $b = 1, b = B$ cases) is provided in supplement. Here $\rho(\cdot)$ is the phase function of the material denoting the probability of turning from one direction to the next one upon interacting with a scatterer, and $\tilde{\alpha}$ is the exponential attenuation along paths in the volume times its redial decay: $\tilde{\alpha}(\mathbf{o}_1, \mathbf{o}_2) = 1/|\mathbf{o}_2 - \mathbf{o}_1| \cdot \exp(-\frac{1}{2}\sigma_t|\mathbf{o}_2 - \mathbf{o}_1|)$. Finally

$$\begin{aligned} &\gamma(\widehat{\bar{\mathbf{o}}_b\bar{\mathbf{o}}_{b+1}} - \widehat{\bar{\mathbf{o}}_{b-1}\bar{\mathbf{o}}_b}) = \\ &\qquad e^{-k^2 D|t| \|\widehat{\bar{\mathbf{o}}_b\bar{\mathbf{o}}_{b+1}} - \widehat{\bar{\mathbf{o}}_{b-1}\bar{\mathbf{o}}_b}\|^2 + ikt(\widehat{\bar{\mathbf{o}}_b\bar{\mathbf{o}}_{b+1}} - \widehat{\bar{\mathbf{o}}_{b-1}\bar{\mathbf{o}}_b}) \cdot \mathbf{U}}, \end{aligned} \tag{14}$$

is the integral of phase variations over all possible motions that the node $\bar{\mathbf{o}}_b$ could have taken. It can be seen that γ is lower when the time difference $|t|$ or the diffusion coefficient D, and thus when larger motion is present the correlation decays. This term is similar to the momentum accumulated by common MC algorithms computing temporal-only correlations [42, 49]. Intuitively this term is smaller when the diffusion coefficient D is larger, since for faster motion the phase variations of the two paths are larger and correlation is lower.

The main difference between our derivation and the classical temporal-only correlation is that we evaluate covariances between two different source-sensor pairs, and therefore the contribution f_b^I of the first/end segments is different. To keep the manuscript concise the exact formula is provided in supplement, however, these are *complex-valued* terms taking into account the phase accumulated along the start/end segments of the paths. For the special case where the two illumination and viewing directions are identical $\mathbf{i}_1 = \mathbf{i}_2, \mathbf{v}_1 = \mathbf{v}_2$, the contribution of the start/end segments in our derivation collapse to the contribution of the central segments in Eq. (13).

In Sec. 4 below we use Monte Carlo path sampling to approximate the covariance integral of Eq. (11). The full justification of this result is provided in supplement. However it can be justified by the two insights illustrated in Fig. 2(a-b).

Naively, to define the field propagating from $\mathbf{i}$ to $\mathbf{v}$ at any time instance one needs to sum the throughput contributions over many paths of the form

$$\mathbf{i} \to \vec{\mathbf{x}}^s\left(t\right) \to \mathbf{v}. \tag{15}$$

The throughput is a complex number with a phase ξ proportional to the path length $\ell(\vec{\mathbf{x}})$:

$$\xi(\vec{\mathbf{x}}(t)) = e^{ik\ell(\vec{\mathbf{x}})}, \tag{16}$$

where $k = 2\pi/\lambda$ is the wavenumber at wavelength λ.

As a result, the covariance between two speckle fields can be expressed as an integral over many pairs of paths: $\vec{\mathbf{x}}^1$ from $\mathbf{i}_1$ to $\mathbf{v}_1$ at time $-t/2$; and path $\vec{\mathbf{x}}^2$ from $\mathbf{i}_2$ to $\mathbf{v}_2$ at time $t/2$. Each path has a contribution whose phase is proportional to the difference between the two path lengths:

$$c_{\vec{\mathbf{x}}^1,\vec{\mathbf{x}}^2}\left(-\tfrac{t}{2},\tfrac{t}{2}\right) \propto \xi\left(\vec{\mathbf{x}}^1\left(-\tfrac{t}{2}\right)\right)\cdot\xi\left(\vec{\mathbf{x}}^2\left(\tfrac{t}{2}\right)\right)^*. \quad (17)$$

If the two paths are sampled independently, they have very different lengths, and hence their contributions would have rather random phases. As complex numbers with random phase average to zero, such pairs do not contribute to the covariance. The first insight in simplifying the covariance path-integral is a central result from the literature [50, 53], detailed in supplement, stating that the covariance integral can be computed by only considering joint pairs of paths that share their central segments

$$\vec{\mathbf{x}}^1\left(-\tfrac{t}{2}\right)=\mathbf{i}_1\to\vec{\mathbf{x}}^s-1/2\vec{\boldsymbol{\Delta}}_t\to\mathbf{v}_1,\quad \vec{\mathbf{x}}^2\left(\tfrac{t}{2}\right)=\mathbf{i}_2\to\vec{\mathbf{x}}^s+1/2\vec{\boldsymbol{\Delta}}_t\to\mathbf{v}_2, \quad (18)$$

where we denote the displacement sequence of the path as $\vec{\boldsymbol{\Delta}}_t = \boldsymbol{\Delta}_{\mathbf{t}1},\ldots,\boldsymbol{\Delta}_{\mathbf{t}B}$. Note that in the above equation we use the same central sequence, but at two different time instances. Such joint path sequences are illustrated in Fig. 2(b). With this restriction the phases of the two paths are more consistent since their central segment has roughly the same length. However, as the particles are moving and the paths are traced in two different time instances, their length can still vary.

By considering the space sub-paths $\vec{\mathbf{x}}^s$ and displacement paths $\vec{\boldsymbol{\Delta}}_t$, we can evaluate the covariance as the integral of contributions from joint path pairs:

$$C^{\mathbf{i}_1,\mathbf{i}_2}_{\mathbf{v}_1,\mathbf{v}_2}\left(-\tfrac{t}{2},\tfrac{t}{2}\right) = \iint c_{\vec{\mathbf{x}}^s,\vec{\boldsymbol{\Delta}}_t}\left(-\tfrac{t}{2},\tfrac{t}{2}\right)\,\mathrm{d}\vec{\boldsymbol{\Delta}}_t\,\mathrm{d}\vec{\mathbf{x}}^s. \quad (19)$$

Unfortunately, the path integral in Eq. (19) cannot be evaluated in closed-form. The second central insight in the simplification of the path-integral is as follows. As the displacement of each node is sampled independently from a Gaussian distribution, at least the integration over displacements can be evaluated in closed-form. In supplement we derive the following analytical expression for the path contribution:

$$c_{\vec{\mathbf{x}}^s}\left(-\tfrac{t}{2},\tfrac{t}{2}\right) = \int c_{\vec{\mathbf{x}}^s,\vec{\boldsymbol{\Delta}}_t}\left(-\tfrac{t}{2},\tfrac{t}{2}\right)\,\mathrm{d}\vec{\boldsymbol{\Delta}}_t = \prod_{b=0}^{B} f_b^I, \quad (20)$$

with the f_b^I defined in Eq. (13). This implies that we can evaluate the covariance by only integrating *static* paths, as illustrated in Fig. 2(c) and outlined in the beginning of this section using Eq. (11). The phase variations resulting from particle motion around each node, are integrated into the momentum $\gamma(\cdot)$.

4. ESTIMATING SPATIO-TEMPORAL SPECKLE COVARIANCES

Our goal is to compute the spatio-temporal covariance of Eq. (11). Given the absence of analytical solution, we want to approximate the integral using importance sampling. For that we sample N paths from a distribution $q(\vec{\mathbf{x}}^s)$ of choice, and approximate the covariance as

$$C^{\mathbf{i}_1,\mathbf{i}_2}_{\mathbf{v}_1,\mathbf{v}_2}\left(-\tfrac{t}{2},\tfrac{t}{2}\right) \approx \frac{1}{N}\sum_{n=1}^{N}\frac{c_{\vec{\mathbf{x}}^{s,n}}\left(-\tfrac{t}{2},\tfrac{t}{2}\right)}{q(\vec{\mathbf{x}}^{s,n})}. \quad (21)$$

While any distribution $q(\vec{\mathbf{x}}^s)$ would provide an unbiased estimate in Eq. (21), the variance of this estimator can be largely reduced using importance sampling rather than naive uniform sampling. The estimation largely improves when we can define a sampling strategy for which q is a good approximation of $c_{\vec{\mathbf{x}}^{s,n}}$. We review below two sampling strategies for the temporal-only case, which are defined by different choices of q. We then adapt them to the case of spatio-temporal covariance.

Computing temporal-only covariance. Previous approaches compute temporal correlation alone without spatial variation of the source and/or sensor position. In this case $\mathbf{i}_1 = \mathbf{i}_2$ and $\mathbf{v}_1 = \mathbf{v}_2$, and the paths $\vec{\mathbf{x}}^1,\vec{\mathbf{x}}^2$ in the derivation of the previous section share all their segments. In particular, the formula for f_b^I (Eq. (13)) is equivalent for all b values, including the first and end segments. We also note that apart from the $\gamma(\widehat{\bar{\mathbf{o}}_b,\bar{\mathbf{o}}_{b+1}}-\widehat{\bar{\mathbf{o}}_{b-1},\bar{\mathbf{o}}_b})$ component, the terms f_b^I essentially define a Markovian path distribution. Thus one way to evaluate Eq. (21) is to use a path-tracing algorithm, sampling N paths $\vec{\mathbf{x}}^{s,n}$ in the following scheme:

1. Sample the first ray $\hat{\omega}_0$ emerging from $\mathbf{i}$.
2. While not hitting the volume boundary, repeat for every successive segment:
   2.1 Sample the next point $\bar{\mathbf{o}}_b$ from a distribution
   $$q(\bar{\mathbf{o}}_b) = \tilde{\alpha}(\bar{\mathbf{o}}_{b-1},\bar{\mathbf{o}}_b)^2\cdot\sigma_s(\bar{\mathbf{o}}_b). \quad (22)$$
   2.2 Sample the next direction $\hat{\omega}_b$ from the distribution
   $$q(\hat{\omega}_b|\bar{\mathbf{o}}_b) = \rho(\hat{\omega}_{b-1}\cdot\hat{\omega}_b). \quad (23)$$
3. If the last node on path $\bar{\mathbf{o}}_B$ is on sensor $\mathbf{v}$, update using Eq. (20)
   $$C^{\mathbf{i},\mathbf{i}}_{\mathbf{v},\mathbf{v}}\left(-\tfrac{t}{2},\tfrac{t}{2}\right) \mathrel{+}= \frac{1}{N}\frac{c_{\vec{\mathbf{x}}^{s,n}}\left(-\tfrac{t}{2},\tfrac{t}{2}\right)}{q(\vec{\mathbf{x}}^{s,n})}. \quad (24)$$

Overall a path in this approach is sampled from a distribution

$$q(\vec{\mathbf{x}}^{s,n}) = q(\hat{\omega}_0|\bar{\mathbf{o}}_0)\prod_{b=1}^{B}q(\bar{\mathbf{o}}_b)q(\hat{\omega}_b|\bar{\mathbf{o}}_b). \quad (25)$$

The contribution of the path $c_{\vec{\mathbf{x}}^{s,n}}$ is non zero, only if it reaches the area of the sensor $\mathbf{v}$, for such cases we note that the ratio $f_b^I/(q(\bar{\mathbf{o}}_b)q(\hat{\omega}_b|\bar{\mathbf{o}}_b))$ is only the $\gamma(\cdot)$ terms. Thus the estimate can be expressed as

$$C^{\mathbf{i},\mathbf{i}}_{\mathbf{v},\mathbf{v}}\left(-\tfrac{t}{2},\tfrac{t}{2}\right) \approx \frac{1}{N}\sum_{\substack{n|\vec{\mathbf{x}}^{s,n}\\ \text{ends in }\mathbf{v}}}\prod_{b=1}^{B}\gamma(\widehat{\bar{\mathbf{o}}_b^n\bar{\mathbf{o}}_{b+1}^n}-\widehat{\bar{\mathbf{o}}_{b-1}^n\bar{\mathbf{o}}_b^n}). \quad (26)$$

Below, we refer to this approach as basic path-tracing. Its main drawback is that if the sensor area is small, the vast majority of paths do not reach the sensor and a lot of computation power is wasted without contributing to the estimate of Eq. (26), see Fig. 3(a).

A more efficient sampling strategy that is commonly used in computer graphics is based on path tracing with *next-event estimation* [54–56], or variance reduction. Rather than waiting for the path to hit the sensor, we explicitly connect the last node to the sensor. As we sample only the first B segments, unlike Eq. (25), the path sampling probability does not include the last segment and can be expressed as

$$q(\vec{\mathbf{x}}^{s,n}) = q(\bar{\mathbf{o}}_B)q(\hat{\omega}_0|\bar{\mathbf{o}}_0)\prod_{b=1}^{B-1}q(\bar{\mathbf{o}}_b)q(\hat{\omega}_b|\bar{\mathbf{o}}_b). \quad (27)$$

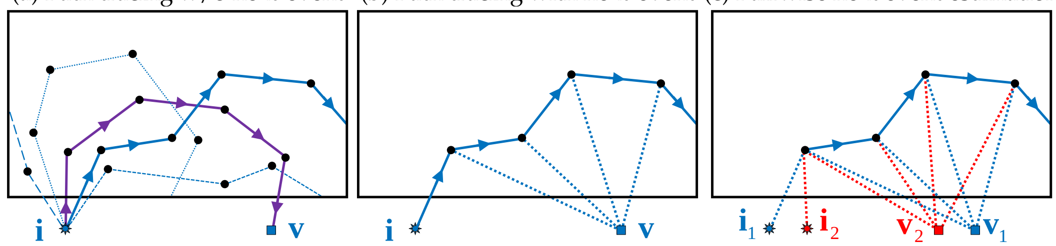

Fig. 3. Path tracing strategies: (a) Basic path tracing samples paths from a Markovian path distribution following Eq. (25). Most paths do not end in the sensor, and they are discarded. (In the figure, only purple curve is contributing and all blue ones are discarded) (b) In a next-event estimation approach all paths contribute to the estimate, and moreover, every node on the path is explicitly connected to the sensor. We weight each connection by the probability that a path-segment leaving that node will actually hit the sensor. (c) Next-event estimation of path pairs: we only sample the central segment of the path, and connect it to two sources and two sensors. The covariance estimate sums the throughput contributed from such connections.

As a result, the covariance estimate can be expressed as

$$C^{\mathbf{i},\mathbf{i}}_{\mathbf{v},\mathbf{v}}\left(-\tfrac{t}{2},\tfrac{t}{2}\right) \approx \frac{1}{N}\sum_n f_B^{I,n}\cdot\prod_{b=1}^{B-1}\gamma(\widehat{\bar{\mathbf{o}}_b^n\bar{\mathbf{o}}_{b+1}^n} - \widehat{\bar{\mathbf{o}}_{b-1}^n\bar{\mathbf{o}}_b^n}). \tag{28}$$

Since we do not sample the last segment, the ratio

$$\frac{c_{\vec{\mathbf{x}}^{s,n}}\left(-\tfrac{t}{2},\tfrac{t}{2}\right)}{q(\vec{\mathbf{x}}^{s,n})} \tag{29}$$

leaves the term $f_B^{I,n}$ in Eq. (28). Note that effectively, the formula for this term provided in supplement is the probability that when sampling a path leaving $\bar{\mathbf{o}}_B$, we will actually sample the segment connecting $\bar{\mathbf{o}}_B$ to the sensor. The main advantage of Eq. (27) over the basic path-tracing approach in Eq. (25) is that *all* paths contribute to the estimate, and estimation noise is considerably reduced. Moreover, since all segments on the path are sampled using importance sampling, we can reuse them and connect to the sensor from every node on the path, not only when it exits the volume, improving path utility, see Fig. 3(b). In supplement we evaluate path tracing with and without next event estimation. We show that for small sensor sizes, next-event estimation provides a very significant acceleration. In practice MC simulations for diffused correlation spectroscopy applications often use wide sensors, and for such, the next-event estimation does not provide additional acceleration. However, as we see below, to extend path-tracing algorithms to the case of spatio-temporal covariances, we need to exploit next-event estimation ideas.

Computing spatio-temporal covariance. To compute spatio-temporal covariance we want to consider two paths that can start and/or end at two different points. In this case the term f_b^I has a different structure at the first and last segments of the path (detailed in supplement), and this expression does not lend itself to simple sampling. As we have seen above, using the next event estimation strategy, there is no need to sample the last segment of the path, but rather include f_B^I in the accumulated contribution. We can use a similar strategy for the first segment. Rather than starting from the source and sampling the length of the first segment, we directly sample the first node $\bar{\mathbf{o}}_1$ and the direction $\hat{\omega}_1$ of the segment $\widehat{\bar{\mathbf{o}}_1,\bar{\mathbf{o}}_2}$ from some distribution q_1 of choice. Subsequent segments are sampled as before. As we do not sample the first segment, we explicitly connect the first node to the source as in Fig. 3(c), and add to the summation its throughput f_0^I:

$$C^{\mathbf{i}_1,\mathbf{i}_2}_{\mathbf{v}_1,\mathbf{v}_2}\left(-\tfrac{t}{2},\tfrac{t}{2}\right) \approx \frac{1}{N}\sum_n \frac{f_0^{I,n}\cdot f_B^{I,n}}{q_1(\bar{\mathbf{o}}_1^n,\hat{\omega}_1^n)}\cdot\prod_{b=1}^{B-1}\gamma(\widehat{\bar{\mathbf{o}}_b^n\bar{\mathbf{o}}_{b+1}^n} - \widehat{\bar{\mathbf{o}}_{b-1}^n\bar{\mathbf{o}}_b^n}), \tag{30}$$

The complete path sampling algorithm is provided in supplement, along with an extension for heterogeneous, spatially varying volumes.

There are multiple ways in which the first node can be sampled, and a good one may depend on the imaging geometry of interest, see discussion in [46]. The simplest strategy is to sample the first node uniformly. Alternatively we can sample it in probability 0.5 from $|\tilde{\alpha}(\mathbf{i}_1,\bar{\mathbf{o}}_1)|^2$ and in probability 0.5 from $|\tilde{\alpha}(\mathbf{i}_2,\bar{\mathbf{o}}_1)|^2$.

5. SAMPLING A SPECKLE FIELD

In this section our goal is to sample a speckle field with the correct spatio-temporal statistics. For that we assume we are given a list of J sources $\mathbf{i}_1,\ldots,\mathbf{i}_J$, sensors $\mathbf{v}_1,\ldots,\mathbf{v}_J$ and time indices $t_1,\ldots,t_J$, and wish to sample J complex numbers $u^{\mathbf{i}_1}_{\mathbf{v}_1},\ldots,u^{\mathbf{i}_J}_{\mathbf{v}_J}$ that have the same covariance as computed in the previous section. That is, for every j,k,

$$\mathrm{E}\left[u^{\mathbf{i}_j}_{\mathbf{v}_j}\cdot {u^{\mathbf{i}_k}_{\mathbf{v}_k}}^*\right] - \mathrm{E}\left[u^{\mathbf{i}_j}_{\mathbf{v}_j}\right]\cdot\mathrm{E}\left[u^{\mathbf{i}_k}_{\mathbf{v}_k}\right]^* = C^{\mathbf{i}_j,\mathbf{i}_k}_{\mathbf{v}_j,\mathbf{v}_k}(t_j,t_k). \tag{31}$$

A straightforward way to do that would be to use the algorithm of the previous section to compute all elements of the $J\times J$ covariance matrix, and then sample our fields as entries of a multi-variate Gaussian distribution. To reduce the computational complexity, we suggest that we can use the subpaths sampled in the Monte-Carlo process to directly generate fields with the desired covariance.

We follow the strategy of the previous section and sample N subpaths $\vec{\mathbf{x}}^{s,n}$. For each subpath we sample a sequence of temporal displacements $\vec{\boldsymbol{\Delta}}^n_{t_j}$ from $\mathcal{T}$. We define $N\times J$ paths by concatenating the same sub-paths to *all* sources and sensors, as illustrated in Fig. 4.

$$\vec{\mathbf{x}}_j^n(t_j) = \mathbf{i}_j \to \vec{\mathbf{x}}^{s,n} + \vec{\boldsymbol{\Delta}}^n_{t_j} \to \mathbf{v}_j. \tag{32}$$

We define the sampled fields as the sum of contributions from these paths. Each path has a phase proportional to its length and we also need to take into account the attenuation and scattering

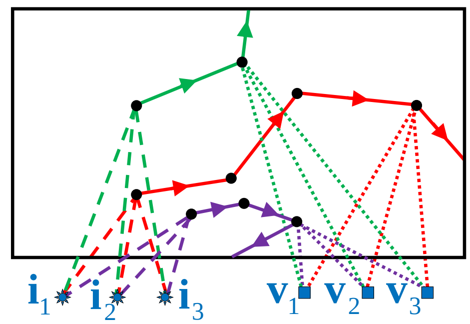

Fig. 4. Sampling speckle fields: We sample subpaths $\vec{\mathbf{x}}^{s,n}$. To achieve a field with consistent entries, each subpath is connected to *all* source and sensors.

amplitude function at the first and last segments, as those are not sampled by q. This leads to the fields

$$u^{\mathbf{i}_j}_{\mathbf{v}_j} = \frac{1}{N}\sum_{n=1}^{N} u^{n,\mathbf{i}_j}_{\mathbf{v}_j}, \tag{33}$$

with

$$u^{n,\mathbf{i}_j}_{\mathbf{v}_j} = \sqrt{\frac{\sigma_s(\bar{\mathbf{o}}^n_1)}{q_1(\bar{\mathbf{o}}^n_1,\hat{\omega}^n_1)}}\, s(\widehat{\mathbf{i}_j,\bar{\mathbf{o}}^n_1}\cdot\widehat{\bar{\mathbf{o}}^n_1,\bar{\mathbf{o}}^n_2})\cdot s(\widehat{\bar{\mathbf{o}}^n_{B-1},\bar{\mathbf{o}}^n_B}\cdot\widehat{\bar{\mathbf{o}}^n_B,\mathbf{v}_j})$$
$$\cdot\,\tilde{\alpha}(\mathbf{i}_j,\bar{\mathbf{o}}^n_1)\cdot\tilde{\alpha}(\bar{\mathbf{o}}^n_B,\mathbf{v}_j)\prod_{b=0}^{B}\xi(\mathbf{o}^n_b(t_j)\to\mathbf{o}^n_{b+1}(t_j)). \tag{34}$$

A detailed pseudo-code for the field-sampling algorithm is provided in supplement. We emphasize that while the central segment $\vec{\mathbf{x}}^{s,n}$ is shared by all paths $\vec{\mathbf{x}}^n_j(t_j)$, the lengths of the start and end segments, connecting the first and last shared node $\mathbf{o}^n_1, \mathbf{o}^n_B$ to different sources and sensors are different, and hence for different entries j of the field the phases of $u^{n,\mathbf{i}_j}_{\mathbf{v}_j}$ are different. However, the fact that the same central segments are used to render all entries of the vector $u^{n,\mathbf{i}_j}_{\mathbf{v}_j}$ leads to consistent speckles. For example, if sensors $\mathbf{v}_1, \mathbf{v}_2$ are located next to each other, the phases of the segments $\xi(\bar{\mathbf{o}}^n_B\to\mathbf{v}_1)$ and $\xi(\bar{\mathbf{o}}^n_B\to\mathbf{v}_2)$ are similar and a smooth speckle grain is generated, as we visualize in the results section below.

In supplement we formally prove that the fields sampled with this strategy have the desired covariance of Eq. (31). Intuitively, this results from the fact that different paths are independent and for each path the expectation of its contribution to the pairs $(\mathbf{i}_j, \mathbf{v}_j), (\mathbf{i}_k, \mathbf{v}_k)$ is the same as the pairwise path contribution we sum in Eq. (28). We also validate this equivalence numerically in the following section.

We emphasize that the fields generated by the algorithm described in this section do not correspond to any physical particle instantiations as simulated in Fig. 1. Yet, they have the same *second order statistics* as fields obtained from a particle instantiation followed by an exact solution to the wave equation. However, the fields sampled with our algorithm do not contain any higher order statistics, such as the C2 and C3 terms in [5]. In supplement we also add to the sampled fields the speckle mean (the ballistic term).

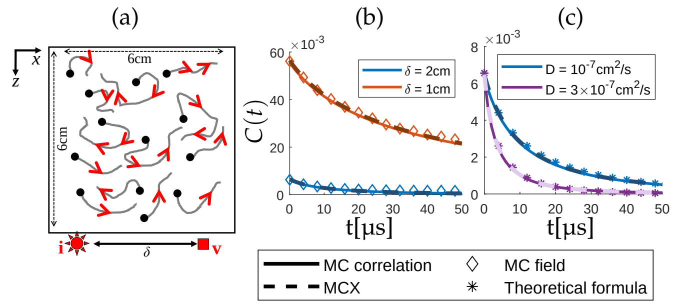

Fig. 5. Validation of temporal-only correlations: we compare our algorithm against the MCX simulator [42], which is designed to compute temporal-only speckle correlations. Our simulator agrees accurately with MCX (dashed MCX curves are barely visible), both when used to compute covariance directly and when used to sample speckle fields. For large source-sensor separation the correlation decay can also be matched with an analytical formula. (a) Illustrating the simulated geometry and medium dimensions. The simulation uses an MFP of 0.1 cm, $\lambda = 500$ nm, isotropic scattering, and the dynamic areas occupy 9% of the overall volume. (b) Evaluating two source-sensor separations δ using $D = 10^{-7}$ cm^2/s and (c) evaluates two diffusion coefficient values using $\delta = 2$ cm.

6. RESULTS

A. Validation

Temporal correlations. In Fig. 5 we start by validating our approach on 3D scenes using the publicly available MCX package [42]. This simulator is aimed at computing temporal-only correlations. In Fig. 5 we plot the temporal-only correlation $C^{\mathbf{i},\mathbf{i}}_{\mathbf{v},\mathbf{v}}(0,t)$ as a function of t. The simulation uses point source/sensors on the volume boundary separated by distance δ. In all cases we compute the correlation directly using the covariance MC sampling algorithm of Sec. 4. We also sample speckle fields using the algorithm of Sec. 5 and compute the temporal correlations of these fields. All three approaches match precisely. We also compare the prediction against the theoretical prediction of correlation decay [57]. This prediction holds only for large source-sensor separations, stating that

$$C(t) = \frac{3}{4\pi l_t}\left(\frac{\exp\left(-\frac{k\cdot r_1}{l_t}\sqrt{6Dt}\right)}{r_1} - \frac{\exp\left(-\frac{k\cdot r_2}{l_t}\sqrt{6Dt}\right)}{r_2}\right) \tag{35}$$

where l_t is the transport MFP, $r_1 = \sqrt{\delta^2 + l_t^2}$, and $r_2 = \sqrt{\delta^2 + (2.33\cdot l_t)^2}$ (ignoring refraction at surface interface).

Spatial correlations. In Fig. 6 we simulate a static scene and plot spatial-only memory effect correlations of the form $C^{\hat{\mathbf{i}},\hat{\mathbf{i}}+\Delta_\theta}_{\hat{\mathbf{v}},\hat{\mathbf{v}}+\Delta_\theta}(0,0)$. That is, we plot the correlation between a field $u^{\hat{\mathbf{i}}}_{\hat{\mathbf{v}}}$ illuminated by a directional source $\hat{\mathbf{i}}$ and a field illuminated by a tilted source at direction $\hat{\mathbf{i}} + \Delta_\theta$. These memory-effect correlations decay as a function of the tilt angle Δ_θ. For thick volumes where the diffusion approximation applies, the correlation decay can be predicted by analytic formulas, known as the C1 term in [5]. In Fig. 6 we plot such correlations for media of two different thicknesses. At all cases we keep the mean free path fixed at 0.3 cm and vary the anisotropy parameter g of the phase function (so that while mean free path is fixed, the transport mean free

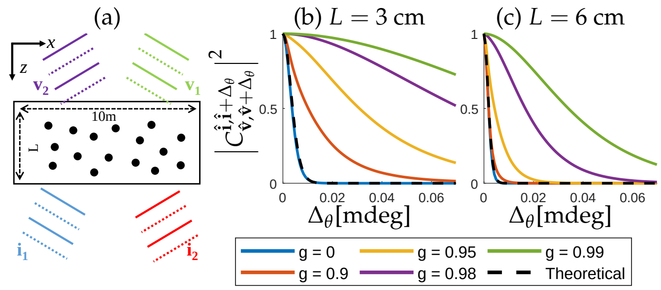

Fig. 6. Spatial-only memory effect correlation between the speckle fields generated from a sample under two directional illuminations, plotted as a function of the tilt Δ_θ between the illumination directions. We plot such correlations for media of two different thicknesses. We keep the mean free path fixed at 0.3 cm and vary the anisotropy parameter g of the phase function (so that while mean free path is fixed, the transport mean free path varies). For the thinner volume our correlation decay agrees with the theoretical C1 prediction at $g = 0$, but differs from it at larger g values as the diffusion limit is not yet achieved. For the thicker sample the diffusion approximation is also valid with $g = 0.9$. The simulation uses $\lambda = 500$ nm.

path varies). For the thinner volume our correlation decay agrees with theoretical prediction at $g = 0$, but differs from it at larger g values as the diffusion limit is not yet achieved. For the thicker sample the diffusion approximation is also valid with $g = 0.9$.

Spatio-temporal correlations. In Fig. 7 we test the accuracy of the spatio-temporal correlations computed by our algorithm. As no Monte Carlo simulator is available we compare against statistics evaluated with an exact wave-solvers [39]. For that we sample many scatterer instantiations as in Fig. 1, solve the wave equation exactly using a numerical solver [39], and compute the empirical correlations as in Eq. (7). We restrict the comparison to flatland as the solver [39] only supports flatland equations. We simulate three different types of scatterer motions, illustrated in Fig. 7(d-f). The first case is Brownian only, the second case is a motion combining both a Brownian and a linear component, and finally we simulate a purely linear motion. In Fig. 7(a) we plot correlations of the form

$$c(\Delta_x, t) \equiv C^{\mathbf{i},\mathbf{i}}_{\mathbf{v},\mathbf{v}+\Delta_x}\left(-\tfrac{t}{2}, \tfrac{t}{2}\right) = \mathrm{E}\left[u^{\mathbf{i}}_{\mathbf{v}}\left(-\tfrac{t}{2}\right) \cdot u^{\mathbf{i}}_{\mathbf{v}+\Delta_x}\left(\tfrac{t}{2}\right)^*\right]. \quad (36)$$

The first row of each correlation image corresponds to the $\Delta_x = 0$ case, which is the usual temporal-only correlation. As can be seen, there are also other correlations in the data which depend on the spatial positions.

In particular, note that if we have a purely linear motion so that for all nodes on a path $\mathbf{\Delta}_{\mathbf{t}b} = t\mathbf{U}$, and we also select $\mathbf{i}_2 - \mathbf{i}_1 = \mathbf{v}_2 - \mathbf{v}_1 = t\mathbf{U}$, i.e. the illumination and viewing directions are "tracking" the particles and are shifted by the exact same amount, then both paths have the exact same length and the correlation should be high. Indeed, when the motion includes a linear component we see a dominant diagonal in the correlation matrix. This corresponds to a situation where the displacement of the sensor point tracks the motion of the scatterers. In the simulation of Fig. 7(a) the illumination is fixed. In Fig. 7(b) we repeat the experiment, this time when the illumination is also shifting in a way that matches the scatterer velocity,

$$c(\Delta_x, t) \equiv C^{\mathbf{i},\mathbf{i}+t\mathbf{U}}_{\mathbf{v},\mathbf{v}+\Delta_x}\left(-\tfrac{t}{2}, \tfrac{t}{2}\right) = \mathrm{E}\left[u^{\mathbf{i}}_{\mathbf{v}}\left(-\tfrac{t}{2}\right) \cdot u^{\mathbf{i}+t\mathbf{U}}_{\mathbf{v}+\Delta_x}\left(\tfrac{t}{2}\right)^*\right]. \quad (37)$$

With this tracking configuration the correlation along the diagonal is even stronger. Finally, in Fig. 7(c) we repeat the simulation using directional illumination. This saves the need of moving the source, and strong correlations are present under a fixed illumination.

For all evaluations in Fig. 7 the correlations produced by our MC simulator match precisely those computed with the exact wave solver, yet our simulator is several orders of magnitude faster and scales to much larger scenes. We also demonstrate that the correlations of fields sampled by the algorithm of Sec. 5 match with the direct covariance evaluation of Sec. 4.

B. Sampling speckle images

Fig. 8 demonstrates speckle images, sampled using our field sampling algorithm described in Sec. 5. Unlike the toy scene of the previous subsection, this sampling algorithm is implemented using a realistic 3D scene.

While these are synthetic images they demonstrate physically consistent correlations. For example, in Fig. 8(b-d), as we tilt the illumination direction, the resulting speckle patterns are correlated shifted versions of each other. Also, in Fig. 8(d-f), the simulated particle motion includes a linear component and a Brownian component, and indeed when we fix the illumination and visualize the speckle variation over time, we can also see how the pattern is shifting. In supplement we demonstrate additional speckle images, sampled with a variety of medium parameters: changing the MFP, changing the phase function, changing the diffusion coefficient, and changing the linear component. In Fig. 8(g-k) we compute the covariances of the sampled fields and compare them with a direct evaluation of the covariance using the algorithm of Sec. 4, showing a precise match. This validates our claim that the field sampling algorithm produces fields with desired covariances. The image simulation includes blurring by the imaging optics following the algorithm of [46], using a numerical aperture of 0.5. As demonstrated below, this algorithm can be used to sample spatio-temporal transmission matrices with physically correct statistics.

C. Application: separating diffused and linear motion components

One important application of measuring temporal correlations is that it can be used to extract information about particle motion. The first approach is to fit the temporal-only correlation formula of Eq. (35) with a parametric model that will allow the estimation of the diffusion coefficient D. However, this formula only describes the correlation as a function of D, and in many contexts [16] there is interest in recovering the flow component $\mathbf{U}$ as well. One way to approach this is with various extended formulas [26, 49] that describe the temporal-only correlation as a parametric function that depends on two parameters corresponding to both D and $\mathbf{U}$. However, as the correlation curve is noisy for large temporal displacements, this approach is not robust.

Alternatively, by exploiting spatio-temporal correlations, we can obtain a richer description of the motion and separate the Brownian (diffused) and linear component. One useful form of spatio-temporal correlation is tracking [58, 59], and our spatio-temporal simulator can help in the design of such systems. To understand tracking, we first note that the linear component $\mathbf{U}$ can be extracted simply by examining speckle images (e.g. Fig. 8) and computing the shift at which correlation is maximized. Given $\mathbf{U}$ we can extract D by computing the temporal

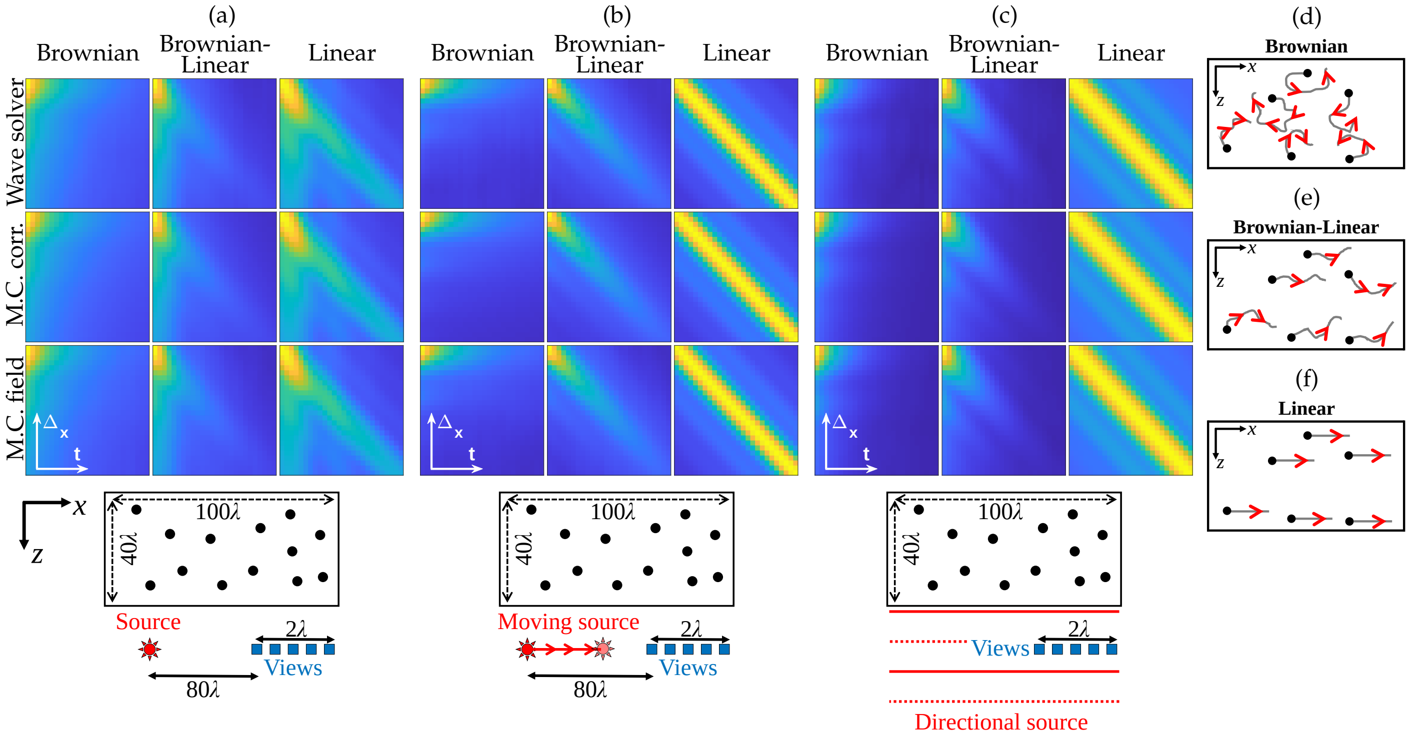

Fig. 7. Spatio-temporal validation: we validate the spatio-temporal covariances predicted by our covariance and field sampling algorithms (Secs. 4 and 5) against covariances computed with an exact wave solver, using Eq. (7). All three approaches produce the exact same covariances. (a) plot spatio-temporal correlations for static illumination, as a function of the displacment between the sensors and the time difference $c(\Delta_x, t) = \mathrm{E}\left[u^{\mathbf{i}}_{\mathbf{v}}\left(\text{-}\frac{t}{2}\right) \cdot u^{\mathbf{i}}_{\mathbf{v}+\Delta_x}\left(\frac{t}{2}\right)^*\right]$. In (b) we also shift the illumination source to track particle motion, demonstrating an even higher correlation. This evaluates $c(\Delta_x, t) = \mathrm{E}\left[u^{\mathbf{i}}_{\mathbf{v}}\left(\text{-}\frac{t}{2}\right) \cdot u^{\mathbf{i}+\Delta_x}_{\mathbf{v}+\Delta_x}\left(\frac{t}{2}\right)^*\right]$. Finally in (c) we simulate correlations under directional illumination, which can detect strong correlations without moving the light source. We simulate three motion types illustrated in (d-f): Brownian only motion, mixture of Brownian and linear motion as well as a linear only motion. For fully linear motion, strong spatio-temporal correlations can be detected over long time instances. The simulation uses an homogeneous MFP$=40\lambda$, $D = 0.015\lambda^2/\mathrm{s}$, $\mathbf{U} = 1\lambda/\mathrm{s}$, Δ_x ranging from 0 to 2λ, and t ranging from 0 to 2s.

correlation of a tracking system, when the illumination and sensor point are shifting with the same velocity as the particles. To see this, note that in a standard temporal-only correlation we would measure:

$$c^{\text{no tracking}}(t) = E\left[u^{\mathbf{i}}_{\mathbf{v}}(0) \cdot u^{\mathbf{i}}_{\mathbf{v}}(t)^*\right], \tag{38}$$

and in a tracking system we measure

$$c^{\text{track}}(t) = E\left[u^{\mathbf{i}}_{\mathbf{v}}(0) \cdot u^{\mathbf{i}+t\mathbf{U}}_{\mathbf{v}+t\mathbf{U}}(t)^*\right]. \tag{39}$$

If both the start and end points as well as all nodes on the path are shifted by $t\mathbf{U}$, the path length is invariant to this shift and is only influenced by the isotropic D component. To demonstrate this, in Fig. 9 we simulated temporal correlations in a moving volume, whose motion includes both $\mathbf{U}$ and D components. We compare the temporal only (no-tracking) correlation curve of this volume to the temporal-only correlation simulated using the same D but $\mathbf{U} = 0$. We see that these two curves are very different and thus, in the presence of a $\mathbf{U}$ component the decay of the curve cannot be used to extract D. In contrast, the tracking curve in the configuration with $\mathbf{U}$ matches precisely the curve of the $\mathbf{U} = 0$ simulation. Thus tracking undoes the influence of the linear flow and allows us to estimate the diffusion coefficient D by fitting the temporal correlation curve.

D. Dynamic wavefront shaping

Wavefront shaping algorithms [38, 60, 61] attempt to overcome tissue scattering and find modulated illumination, which is aberrated in a way that is conjugate to the tissue aberration. When propagating through a scattering medium, the two aberrations should cancel each other and all light energy is focused into a sharp spot. Despite the large potential of wavefront shaping ideas in overcoming tissue scattering, every tissue sample would require its own unique modulation, and the estimation of such a modulation is a time consuming optimization. This is particularly challenging with dynamic samples as the modulation should rapidly adapt to the change in the tissue. Recently Blochet *et al.* [47] have experimentally tested the operation of wavefront shaping algorithms in mediums that contain a mixture of static and dynamic parts. They arrive at the interesting observation that iterative wavefront shaping algorithms, e.g. in an Hadamard basis [62], tend to estimate modulations that adapt to the static part of the volume and hence they are more robust to temporal variations. The authors explain this by the fact that the modulation estimation algorithm relies on iterations that project a modulation estimate onto the scattering medium and re-update the modulation based on the intensity measured at the desired focal spot. Due to the iterative nature of this algorithm, the dynamic part that is changing between measurements is

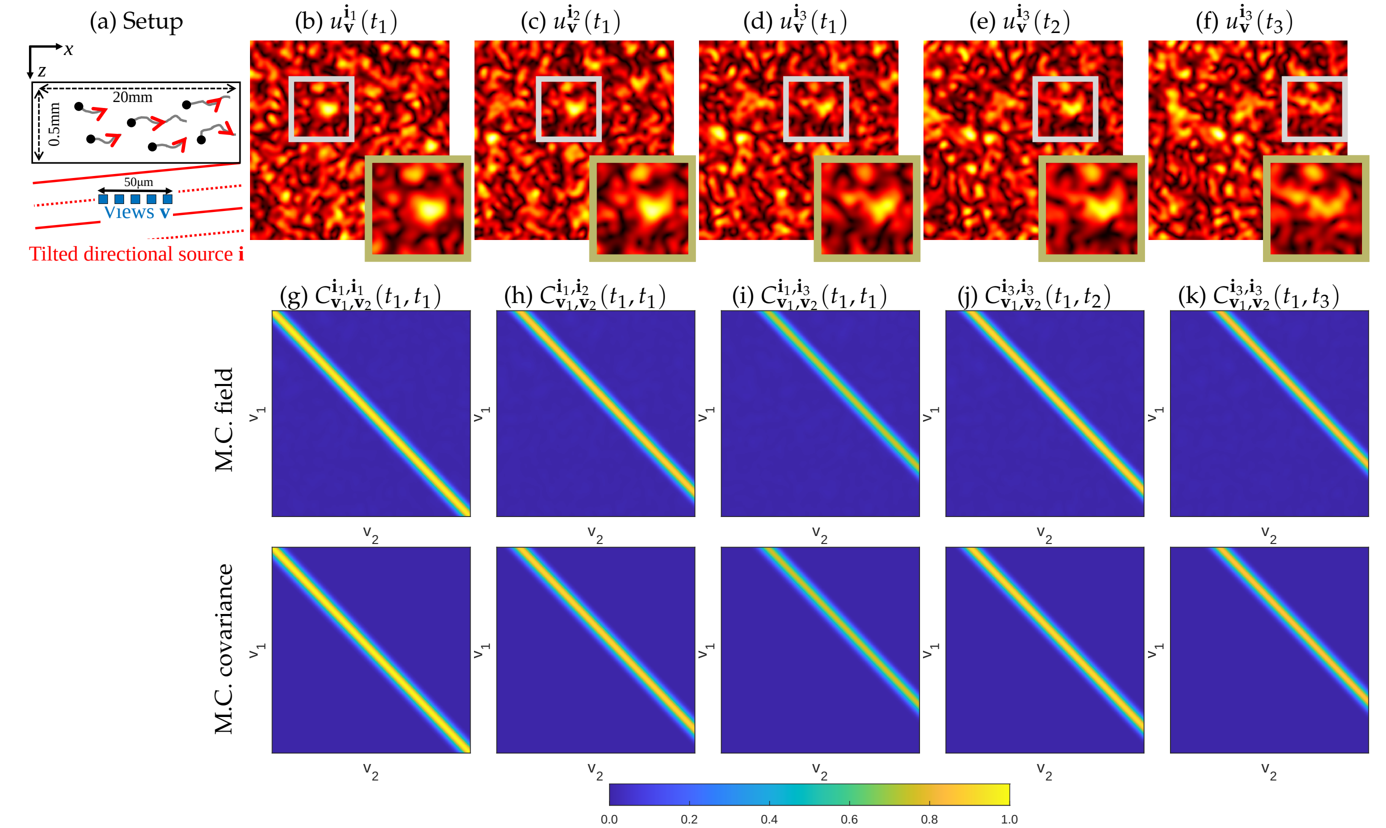

Fig. 8. Sampling speckle images: we use the algorithm of Sec. 5 to sample speckle images with consistent spatio-temporal variations. (a) imaging setup. (b-d) Three speckle images under different illumination directions. Note how the speckles shift with illumination angle, demonstrating memory effect correlations. (d-f) temporal variation of the speckle pattern for a fixed illumination. Again, due to the linear component, the speckle patterns are shifting. In (g-k) we compute the covariances of the sampled fields and compare them with a direct evaluation of the covariance using the algorithm of Sec. 4 showing that our sampled fields follow the desired covariances. In our simulation the volume is illuminated by a plane wave starting at $\hat{\mathbf{i}}_1 = 0°$ and tilting at angular intervals of 0.007°. The simulated motion includes a mixture of linear and Brownian components with $\mathbf{U}_x = 25$ cm/s, $D = 2 \times 10^{-8}$ cm^2/s. Temporal images are sampled at intervals of 25 µs. We use MFP = 250 µm and isotropic scattering. Images are simulated with a 0.5 NA.

manifested as noise to the optimization, and mostly the static part is fitted. The observation of Blochet *et al.* [47] is based on experimental validation, which is limited to a particular setup. With our simulation we can obtain the same results numerically and test them over a wide range of imaging and material parameters. To this end we exploit the fact that we can sample physically-consistent speckle fields as a function of illumination, spatial sensing point and time, which is effectively the sampling of a spatio-temporal transmission matrix.

The setup of our simulation is illustrated in Fig. 10(a). A coherent wavefront is modulated by an SLM with 1024 modes. A camera is located at the back side of the sample and can monitor the amount of energy at the desired focal spot, as well as its temporal variation. We record the intensity I_{Focus} at one pixel of the validation camera for 2 seconds and use these measurements to update the SLM modulation following the algorithm described by [63]. After 2 seconds, we stop to update the SLM and record the resulting intensity $I_{\text{Focus}}(t)$ for additional 4 seconds. We also record the native temporal intensity variations $I_{\text{Speckle}}(t)$ at the same pixel for 4 seconds without applying any SLM modulation. We compute the temporal intensity correlation as evaluated by [47]:

$$g_2(t) = \frac{\mathrm{E}_\tau \left[I(\tau) \cdot I(t+\tau) \right]}{\mathrm{E}_\tau \left[I(\tau) \right]^2}. \tag{40}$$

We compute this temporal correlation for both focus and speckle intensities. To reduce noise we average the correlations of 100 different transmission matrix realizations. We demonstrate in Fig. 10(b-c) some of these correlations. As predicted by [47], the intensity measured after a focusing modulation is computed, is more stable compared to the native speckle variation in an unmodulated setting, and the decay of the correlation as a function of time is lower. This observation is consistent for different motion speeds and different MFP densities. As also observed by [47], when the scatterers density in the dynamic part increases, this layer induces more scattering and hence the decay of the correlation is faster even after we find a focusing modulation.

To analyze the decay analytically, we follow [47] and fit the normalized speckle temporal covariance with a parametric model of the form

$$g_2(t) = 1 + w \left| g_1(t) \right|^2, \tag{41}$$

$$\left| g_1(t) \right|^2 \approx \exp\left(\frac{-2t}{\Gamma} \right) \cdot \left(1 + t^2 \cdot \frac{\sigma_\Gamma^2}{2} \right)^2, \tag{42}$$

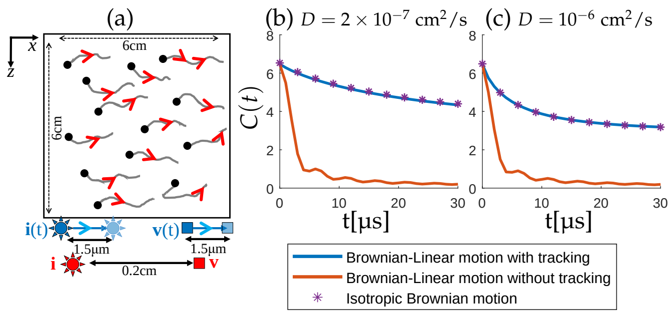

Fig. 9. Separating motion components. We demonstrate the temporal decay in correlation for a static source and sensor, compared with the case where they are both shifting to track the linear part of the motion velocity. Without tracking the correlation decay mixes both a Brownian and a linear motion components. When tracking is used, the remaining correlation is only a function of the Brownian component. It precisely matches the correlation observed in a volume with the same D parameter and no linear term ($\mathbf{U} = 0$). The simulation uses isotropic scattering, MFP $= 0.1$ cm, $\lambda = 500$ nm, a linear motion velocity of $\mathbf{U}_x = 5$ cm/s, and two different Brownian motions simulated in the two sub-figures.

where $g_1(t)$ is the normalized temporal covariance of the complex fields, which is expressed earlier in this paper as $\frac{C^{\mathbf{i},\mathbf{i}}_{\mathbf{v},\mathbf{v}}(0,t)}{C^{\mathbf{i},\mathbf{i}}_{\mathbf{v},\mathbf{v}}(0,0)}$.

Intuitively, w is the dynamic portion of the volume, and when this portion is larger the temporal correlation decays faster. In Fig. 10(d-e), we display the average $1 - w$ and Γ values, respectively. In Fig. 10(d), we see that the dynamic wavefront shaping process achieves a larger static component, indicating that this process strengthens the static path contributions over the paths that have nodes on the dynamic part of the medium. Also, in Fig. 10(e), the decay of the correlation is slower in the focused configuration, indicated by a wider variance Γ.

7. CONCLUSION

This paper derives a Monte Carlo framework for evaluating the spatio-temporal correlations of speckle patterns formed under coherent illuminations. It also offers the ability to sample speckle fields with correct covariances, which can be used for the realization of spatio-temporal transmission matrices. This can be valuable for the design of new imaging algorithms, in particular for generating large-scale training datasets for machine-learning algorithms, bypassing painful lab acquisitions. While we have demonstrated some applications, we have only scratched the surface of what can be done with spatio-temporal statistics and we hope this new simulation framework will motivate future exploration.

At the moment our proof of concept implementation is not as fast as MCX [42]. We hope that some of the ideas introduced for temporal-only MC [44, 64, 65], as well as incoherent path tracing ideas developed in computer graphics [54–56], can be incorporated into an efficient spatio-temporal MC simulator.

REFERENCES

1. J. W. Goodman, *Speckle Phenomena in Optics: Theory and Applications* (Roberts and Company Pub., 2007).
2. R. K. Erf, "Speckle metrology," (Elsevier, 1978).
3. P. Jacquot and J.-M. Fournier, *Interferometry in Speckle Light* (Springer, 2000).
4. G. H. Kaufmann, *Advances in Speckle Metrology and Related Techniques* (Wiley, 2011).
5. E. Akkermans and G. Montambaux, *Mesoscopic Physics of Electrons and Photons* (Cambridge University Press, 2007).
6. J. H. Li and A. Z. Genack, "Correlation in laser speckle," Phys. Rev. E (1994).
7. R. Berkovits and S. Feng, "Correlations in coherent multiple scattering," Phys. Reports (1994).
8. S. Feng, C. Kane, P. A. Lee, and A. D. Stone, "Correlations and fluctuations of coherent wave transmission through disordered media," Phys. Rev. Lett. (1988).
9. I. Freund, M. Rosenbluh, and S. Feng, "Memory effects in propagation of optical waves through disordered media," Phys. Rev. Lett. (1988).
10. G. Osnabrugge, R. Horstmeyer, I. N. Papadopoulos, B. Judkewitz, and I. M. Vellekoop, "Generalized optical memory effect," Optica (2017).
11. B. Judkewitz, R. Horstmeyer, I. Vellekoop, and C. Yang, "Translation correlations in anisotropically scattering media," Nat. Phys. (2014).
12. D. A. Boas and A. G. Yodh, "Spatially varying dynamical properties of turbid media probed with diffusing temporal light correlation," J. Opt. Soc. Am. A (1997).
13. S. Xin, S. Nousias, K. Kutulakos, A. C. Sankaranarayanan, S. Narasimhan, and I. Gkioulekas, "A theory of Fermat paths for non-line-of-sight shape reconstruction," CVPR (2019).
14. R. L. Dougherty, B. J. Ackerson, N. M. Reguigui, F. Dorri-Nowkoorani, and U. Nobbmann, "Correlation transfer: Development and application," JQSRT (1994).
15. B. J. Berne and R. Pecora, *Dynamic light scattering: with applications to chemistry, biology, and physics* (Courier Corporation, 2000).
16. T. Durduran, R. Choe, W. B. Baker, and A. G. Yodh, "Diffuse optics for tissue monitoring and tomography," Reports on Prog. Phys. (2010).
17. D. J. Pine, D. A. Weitz, P. M. Chaikin, and E. Herbolzheimer, "Diffusing wave spectroscopy," Phys. review letters (1988).
18. J. Sutin, B. Zimmerman, D. Tyulmankov, D. Tamborini, K. C. Wu, J. Selb, A. Gulinatti, I. Rech, A. Tosi, D. A. Boas, and M. A. Franceschini, "Time-domain diffuse correlation spectroscopy," Optica (2016).
19. M. Pagliazzi, S. K. V. Sekar, L. Colombo, E. Martinenghi, J. Minnema, R. Erdmann, D. Contini, A. D. Mora, A. Torricelli, A. Pifferi, and T. Durduran, "Time domain diffuse correlation spectroscopy with a high coherence pulsed source: in vivo and phantom results," Biomed. Opt. Express (2017).
20. L. Gagnon, M. Desjardins, J. Jehanne-Lacasse, L. Bherer, and F. Lesage, "Investigation of diffuse correlation spectroscopy in multi-layered media including the human head," Opt. Express (2008).
21. W. B. Baker, A. B. Parthasarathy, D. R. Busch, R. C. Mesquita, J. H. Greenberg, and A. G. Yodh, "Modified Beer-Lambert law for blood flow." Biomed. optics express (2014).
22. E. Buckley, A. Parthasarathy, P. Grant, A. Yodh, and M. Franceschini, "Diffuse correlation spectroscopy for measurement of cerebral blood flow: future prospects," Neurophotonics (2014).
23. S. Yuan, A. Devor, D. A. Boas, and A. K. Dunn, "Determination of optimal exposure time for imaging of blood flow changes with laser speckle contrast imaging," Appl. optics

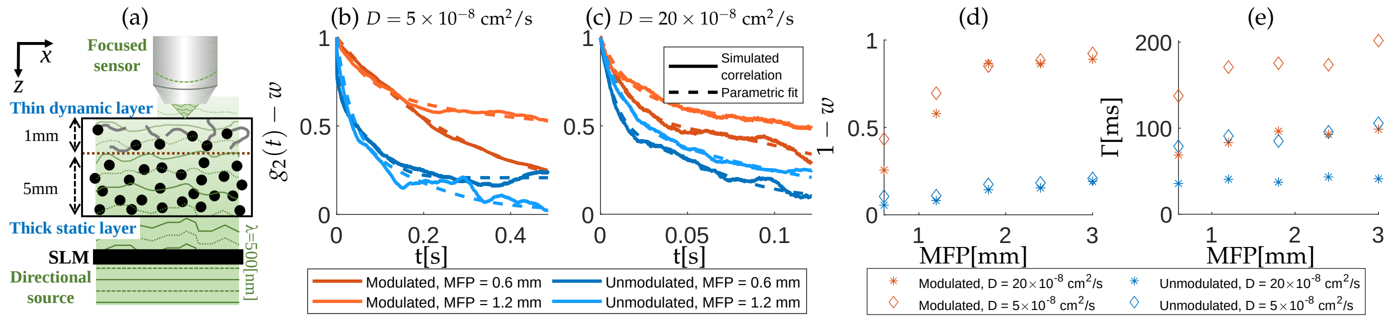

Fig. 10. Dynamic wavefront shaping: we repeat the experiments of [47] with our numerical simulator. (a) Imaging geometry: the volume includes a static layer and a dynamic one, the MFP of the static layer is 0.7 mm and the MFP of the dynamic layer is varied as reported above. An iterative estimation of a wavefront shaping modulation effectively treats the dynamic layer as noise, and mostly adapts to the static part of the volume. (b,c) The decay in correlation after a wavefront-shaping modulation is found is slower than the native decay of the correlation with no modulation. This holds for different diffusion coefficients (different Brownian motion rates) and different densities in the dynamic layer (different MFP). (d-e) we fit the decay with the analytical model in Eq. (41) and Eq. (42) and report the $1 - w$ and Γ values, demonstrating again that the corrected modulation is decorrelating more slowly, as it has originally adapted to the static part of the volume. In the simulation, the camera samples the speckle field at intervals of 243 µs.

(2005).
24. P. Miao, H. Lu, Q. Liu, Y. Li, and S. Tong, "Laser speckle contrast imaging of cerebral blood flow in freely moving animals," J. biomedical optics (2011).
25. W. I. Goldburg, "Dynamic light scattering," Am. J. Phys. (1999).
26. A. B. Leung, K. I. Suh, and R. R. Ansari, "Particle-size and velocity measurements in flowing conditions using dynamic light scattering," Appl. Opt. (2006).
27. O. Katz, P. Heidmann, M. Fink, and S. Gigan, "Non-invasive single-shot imaging through scattering layers and around corners via speckle correlation," Nat. Photonics (2014).
28. J. Bertolotti, E. G. van Putten, C. Blum, A. Lagendijk, W. L. Vos, and A. P. Mosk, "Non-invasive imaging through opaque scattering layers," Nature (2012).
29. K. T. Takasaki and J. W. Fleischer, "Phase-space measurement for depth-resolved memory-effect imaging," Opt. Express (2014).
30. E. Edrei and G. Scarcelli, "Optical imaging through dynamic turbid media using the Fourier-domain shower-curtain effect," Optica (2016).
31. E. Edrei and G. Scarcelli, "Memory-effect based deconvolution microscopy for super-resolution imaging through scattering media," Sci. Reports (2016).
32. M. Hofer, C. Soeller, S. Brasselet, and J. Bertolotti, "Wide field fluorescence epi-microscopy behind a scattering medium enabled by speckle correlations," Opt. Express (2018).
33. T. Wu, J. Dong, X. Shao, and S. Gigan, "Imaging through a thin scattering layer and jointly retrieving the point-spread-function using phase-diversity," Opt. Express (2017).
34. T. Wu, J. Dong, and S. Gigan, "Non-invasive single-shot recovery of a point-spread function of a memory effect based scattering imaging system," Opt. Lett. (2020).
35. X. Wang, X. Jin, and J. Li, "Blind position detection for large field-of-view scattering imaging," Photon. Res. (2020).
36. J. Chang and G. Wetzstein, "Single-shot speckle correlation fluorescence microscopy in thick scattering tissue with image reconstruction priors," J. Biophotonics (2018).
37. M. Alterman, E. Saiko, and A. Levin, "Direct acquisition of volumetric scattering phase function using speckle correlations," in *SIGGRAPH Asia 2022 Conference Papers*, (2022).
38. R. Horstmeyer, H. Ruan, and C. Yang, "Guidestar-assisted wavefront-shaping methods for focusing light into biological tissue," Nat. Photonics (2015).
39. B. Thierry, X. Antoine, C. Chniti, and H. Alzubaidi, "μ-diff: An open-source MATLAB toolbox for computing multiple scattering problems by disks," Comput. Phys. Commun. (2015).
40. K. Yee, "Numerical solution of initial boundary value problems involving Maxwell's equations in isotropic media," IEEE TAP (1966).
41. B. E. Treeby and B. T. Cox., "k-wave: MATLAB toolbox for the simulation and reconstruction of photoacoustic wave-fields," JBO (2010).
42. Q. Fang and D. A. Boas, "Monte Carlo simulation of photon migration in 3D turbid media accelerated by graphics processing units," Opt. Express (2009).
43. Z. Wertheimer, C. Bar, and A. Levin, "Towards machine learning for heterogeneous inverse scattering in 3D microscopy," Opt. Express (2022).
44. S. Xu *et al.*, "Imaging dynamics beneath turbid media via parallelized single-photon detection," Adv. Sci. (2022).
45. C. Bar, M. Alterman, I. Gkioulekas, and A. Levin, "A Monte Carlo framework for rendering speckle statistics in scattering media," ACM TOG (2019).
46. C. Bar, I. Gkioulekas, and A. Levin, "Rendering near-field speckle statistics in scattering media," ACM TOG (2020).
47. B. Blochet, K. Joaquina, L. Blum, L. Bourdieu, and S. Gigan, "Enhanced stability of the focus obtained by wavefront optimization in dynamical scattering media," Optica (2019).
48. B. Bitterli, S. Ravichandran, T. Müller, M. Wrenninge, J. Novák, S. Marschner, and W. Jarosz, "A radiative transfer framework for non-exponential media," ACM Trans. Graph. (2018).
49. D. Boas, S. Sakadzic, J. Selb, P. Farzam, M. Franceschini, and S. Carp, "Establishing the diffuse correlation spectroscopy signal relationship with blood flow." Neurophotonics (2016).
50. A. Ishimaru, *Wave propagation and scattering in random media*, vol. 12 (John Wiley & Sons, 1999).
51. V. Twersky, "On propagation in random media of discrete

scatterers," Proc. Symp. Appl. Math (1964).
52. M. I. Mishchenko, L. D. Travis, and A. A. Lacis, *Multiple Scattering of Light by Particles: Radiative Transfer and Coherent Backscattering* (Cambridge University Press, 2006).
53. M. Mishchenko, L. Travis, and A. Lacis, *Multiple scattering of light by particles: radiative transfer and coherent backscattering* (Cambridge University, 2006).
54. P. Dutre, K. Bala, and P. Bekaert, *Advanced Global Illumination* (A K Peters, Natick, MA, 2006).
55. J. Novak, I. Georgiev, J. Hanika, and W. Jarosz, "Monte Carlo methods for volumetric light transport simulation," Comput. Graph. Forum (2018).
56. E. Veach, "Robust Monte Carlo methods for light transport simulation," Ph.D. thesis, Stanford Uni. (1997).
57. A. Kienle and M. S. Patterson, "Improved solutions of the steady-state and the time-resolved diffusion equations for reflectance from a semi-infinite turbid medium," J. Opt. Soc. Am. A (1997).
58. R. Adrian, "Particle-imaging techniques for experimental fluid mechanics," Annu. review fluid mechanics (1991).
59. M. M. Qureshi, Y. Liu, K. D. Mac, M. Kim, A. M. Safi, and E. Chung, "Quantitative blood flow estimation in vivo by optical speckle image velocimetry," Optica (2021).
60. H. Yu, J. Park, K. Lee, J. Yoon, K. Kim, S. Lee, and Y. Park, "Recent advances in wavefront shaping techniques for biomedical applications," Curr. Appl. Phys. (2015).
61. S. Gigan, O. Katz *et al.*, "Roadmap on wavefront shaping and deep imaging in complex media," J. Physics: Photonics (2021).
62. S. M. Popoff, A. Aubry, G. Lerosey, M. Fink, A. C. Boccara, and S. Gigan, "Exploiting the time-reversal operator for adaptive optics, selective focusing, and scattering pattern analysis," Phys. Rev. Lett. (2011).
63. B. Blochet, L. Bourdieu, and S. Gigan, "Focusing light through dynamical samples using fast continuous wavefront optimization," Opt. Lett. (2017).
64. D. D. Postnov, J. Tang, S. E. Erdener, K. Kılıç, and D. A. Boas, "Dynamic light scattering imaging," Sci. Adv. (2020).
65. B. Lee, O. Sosnovtseva, C. M. Sørensen, and D. D. Postnov, "Multi-scale laser speckle contrast imaging of microcirculatory vasoreactivity," Biomed. Opt. Express (2022).